Hindawi
International Journal of Energy Research
Volume 2024, Article ID 4009198, 14 pages
https://doi.org/10.1155/2024/4009198

Research Article

Hydrogen Storage Capacity of Lead-Free Perovskite NaM_TH_3 (M_T=Sc, Ti, V): A DFT Study

Zia ur Rehman,[1] **Muhammad Awais Rehman**,[2] **Suliman Yousef Alomar**,[3] **Bushra Rehman**,[4] **Muhammad Awais**,[1] **Mahnoor Amjad**,[1] **Surajudeen Sikiru**,[5] **Esraa Mousa Ali**,[6] **and Abu Hamad**[7]

[1]*Department of Mathematics, Namal University, 30 km Talagang Road, 42250 Mianwali, Pakistan*
[2]*Institute of Physics, University of Silesia, ul. 75 Pulku Piechoty 1, 41-500 Chorzow, Poland*
[3]*Zoology Department, College of Science, King Saud University, Riyadh-11451, Saudi Arabia*
[4]*Department of Environmental Science, Quaid-i-Azam University Islamabad, Islamabad 45320, Pakistan*
[5]*School of Physics and Materials Studies, Faculty of Applied Science, Universiti Teknologi Mara, 40450 Shah Alam, Selangor, Malaysia*
[6]*Faculty of Aviation Science, Amman Arab University, 2234, Amman 11953, Jordan*
[7]*Department of Civil, Geological and Mining Engineering (CGM), École Polytechnique de Montréal, Montréal, Canada*

Correspondence should be addressed to Zia ur Rehman; zia545@gmail.com

Received 30 November 2023; Revised 3 January 2024; Accepted 30 January 2024; Published 28 February 2024

Academic Editor: Semen Klyamkin

Hydrogen is a promising clean energy carrier, but its storage is challenging. In this study, we investigate the potential of NaM_TH_3 (M_T=Sc, Ti, V) hydride perovskite as solid-state hydrogen storage material. Using density functional theory (DFT), we comprehensively analyze their structural, hydrogen storage, phonon, electronic, elastic, and thermodynamic properties. Mechanical stability is assessed through calculation of lattice parameters, bulk and shear moduli, Poisson's ratio, and Young's modulus based on elastic constants. All three hydrides were found to be stable mechanically. Furthermore, the anisotropy factor was also investigated. Results show that the investigated hydrides are brittle and metallic. Their metallic character is due to the significant interplay between phonons and electrons. We also investigated their enthalpy, entropy, free energy, Debye temperatures, and specific heat capacities to investigate thermal stability.

1. Introduction

Hydrogen is considered one of the most promising sustainable energy sources compared to conventional fossil fuels like oil, coal, and natural gas [1]. Using solid-state materials as a hydrogen storage medium is one of the most desired solutions [2]. There are two types of solid-state hydrogen storage: physisorption and chemisorption. Using weak van der Waals forces, hydrogen molecules are adsorbed onto the surface of a material, a process known as physisorption. In chemisorption, hydrogen molecules are chemically attached to the surface of a material. Compared to physisorption, chemisorption has a larger theoretical storage capacity but has higher activation energy needed for adsorption and desorption [3–5]. Hydrogen is a possible alternative fuel with its high energy density and green attributes. Hydrogen storage utilizing hydrides, such as magnesium hydride, has been considered an alternate energy storage method. Due to the high gravimetric capacity of such materials, this approach is especially promising. The hydrogen storage capacities per unit mass of perovskite hydrides are typically lower than those of conventional metal hydrides. However, they also

have other benefits that make them viable options in certain scenarios like high volumetric density, tunability, improved kinetics, and reversibility [6]. Hydrogen storage, however, remains an important challenge due to higher desorption temperature and slow kinetics [7, 8]. Due to distinct crystal structures and adaptable characteristics, perovskite materials have been recognized as promising candidates among numerous materials. The general formula for perovskite materials is ABX_3 [9] where A denotes a large cation, B denotes a smaller cation, and X denotes an anion. As A, B, or X may be modified to accommodate additional elements, the cubic crystal symmetry of the perovskite structure makes it a flexible material for a wide range of applications. Substituting hydrogen for X, a hydride perovskite with the general formula ABH_3 is formed. The possible formulas for perovskite-type hydrides are $A^{+1}B^{+2}H_3$ and $A^{+2}B^{+1}H_3{}^{-1}$. Since A and B belong to alkali or alkaline earth metals, the possible hydride structures are limited [10–12]. Hydride perovskites are gaining attention as a promising solution for hydrogen storage. Materials used for hydrogen storage usually have robust hydrogen bonding, wide interstitial spaces for substantial hydrogen storage, catalytic nature for improved hydrogen absorption, and adequate gravimetric hydrogen storage capacities [10, 13]. Such hydride perovskite has different gravimetric storage capacities with gravimetric and volumetric capacities of up to 6 wt% and 88 kg/m^3 depending on the choice of A and B up to six weight percent; therefore, single perovskite materials are the most investigated compounds for hydrogen storage applications [14, 15]. Due to their special qualities, Na-based perovskite materials have recently received a lot of interest; in this series of hydrides, $NaMgH_3$ became the prime focus of research [10, 16]. Surucu et al. studied the formation energy, mechanical stability, thermodynamics, and bulk modulus of NaM_TH_3 (M_T=Co, Fe, Mn) and found the gravimetric storage capacities 3.74 wt%, 3.70 wt%, and 3.57 wt% for $NaMnH_3$, $NaFeH_3$, and $NaCoH_3$, respectively, using DFT [17, 18]. Gencer et al. calculated the electronic, elastic, thermal, and hydrogen storage properties of $NaNiH_3$ with a gravimetric storage capacity of 3.5 wt% [10, 19]. Inspired by these studies, NaM_TH_3 (M_T=Sc, Ti, V) first-principle calculations were carried out at atmospheric pressure and temperature. According to the author's knowledge, there have been no previous reports, and this work is the first detailed investigation of the crystal structure, phonon dispersion curves, gravimetric ratio, and electronic, mechanical, and thermal properties of NaM_TH_3 (M_T=Sc, Ti, V) lead-free hydride perovskites using DFT for hydrogen storage applications. The results of this study will be helpful for future works. The manuscript introduces the study, describes methods for calculations, discusses the results, and finally concludes the study in separate sections.

2. Computational Methodology

Computational work was performed in the domain of density functional theory (DFT) using plane wave pseudopotential approach of CASTEP and Quantum ESPRESSO code to investigate the properties of NaM_TH_3 (M_T=Sc, Ti, V) [20]. The exchange-correlation approximation was done using the Perdew-Burke-Ernzerhof (PBE) parameterization of the generalized gradient approximation (GGA) algorithm [14, 21]. The 3D crystal structures and visualization job were done using VESTA. Equilibrium lattice parameters were determined by fitting the Birch-Murnaghan equation of state-to-energy-volume (E-V) curves, calculated using Quantum ESPRESSO. Unit cell optimization was carried out using the BFGS algorithm integrated within CASTEP. The interaction of valence electrons with the ion core was addressed using the norm-conserving pseudopotential. Pseudoatomic calculations were executed for Na$2s^2$ $2p^6$ $3s^1$, Ti $3s^2 3p^6$ $3d^2$ $4s^2$, V $3s^2$ $3p^6$ $3d^3$ $4s^2$, $3s^2$ $3p^6$ $3d^1$ $4s^2$, and H $1s^1$. The finite displacement method explored dynamic stability using phonon dispersion curves. Thermodynamic properties were computed using the supercell approach. For PDOS calculation on the supercell, an $8 \times 8 \times 8k$-point mesh was employed, ensuring error reduction below 0.01 eV [22, 23]. A separation of 0.015 1/Å between k-points was used to construct the phonon dispersion curve. The total energy convergence was assessed with plane wave cutoff energy 990 eV and $4 \times 4 \times 4$ grid for k-point sampling. Energy calculations and geometry optimization utilized parameters including (a) maximum displacement tolerance 5×10^{-4} Å, (b) maximum stress of 0.02 GPa, (c) maximum tolerance for force 1×10^{-2} eV/Å, and (d) maximum energy 5×10^{-6} eV/atom [24–26].

3. Result and Discussion

3.1. Structural Analysis. Figure 1 shows the cubic crystal structure of the NaM_TH_3 (M_T=Sc, Ti, V) hydride perovskite with the space group of (Pm-3m, 221). The crystal formation was within a cubic unit cell such that the Na atoms were positioned at the corners of the unit cell with coordinates at the origin (0, 0, 0). At the same time, M_T atoms were accurately located at the body center of the unit cell at coordinates (0.5, 0.5, 0.5). The center of each face of the unit cell was clearly marked by the presence of H atoms, notably at the coordinates (0.5, 0, 0), (0, 0.5, 0), and (0, 0, 0.5). To seek the lattice parameters leading to the lowest energy of the structure, we changed the lattice constant a for the NaM_TH_3 (M_T=Sc, Ti, V) hydride perovskites. The unit's volume also changed with the modification of the lattice parameter. To investigate how the unit cell's total energy changes with changes in volume, we used density functional theory (DFT) to calculate forces. The Perdew-Burke-Ernzerhof (GGA-PBE) functional from the generalized gradient approximation was used to calculate the self-consistent field (SCF) energy, and the Broyden-Fletcher-Goldfarb-Shanno (BFGS) algorithm was used for optimization. The system relaxed until the forces exerting pressure on the atoms were insignificant.

E-V curves, as shown in Figure 2, were drawn by plotting volume against the total energies represented by scattered points; curve fitting was done using the Birch-Murnaghan equation of state defined by Eq. (1), and continuous lines show how data fits using the B-M equation. The lowest

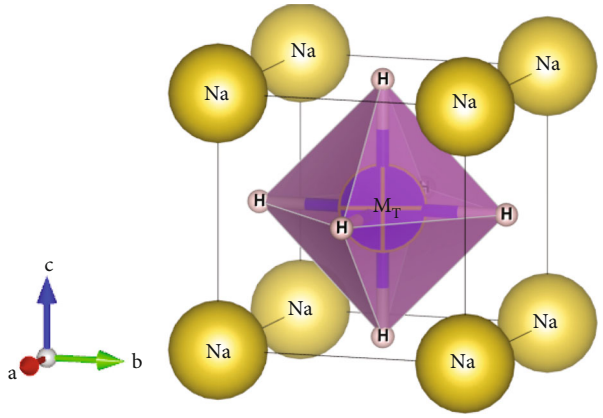

FIGURE 1: The crystal structure of NaM_TH_3 (M_T=Sc, Ti, V).

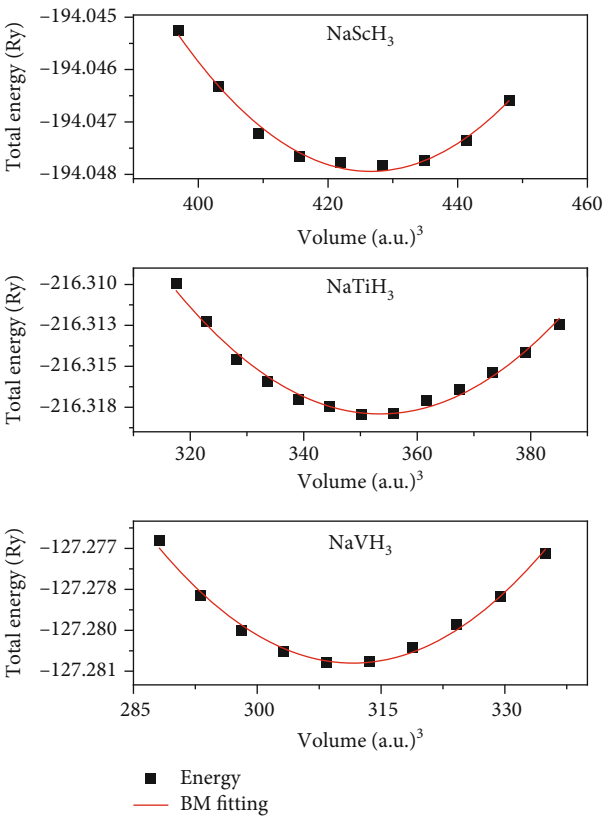

FIGURE 2: The calculated energy-volume (E-V) curves of $NaMTH_3$ (M_T=Sc, Ti, V).

energy value on these curves indicates an equilibrium state that is the most stable.

$$E_{\text{total}}(V) = E_o(V) + \frac{B_o V}{B'\left(B'-1\right)}\left[B_o\left(1-\frac{V_o}{V}\right) + \left(\frac{V_o}{V}\right)^{B'} - 1\right]. \quad (1)$$

In the context of this research, the term $E(V)$ refers to the material's energy at a particular volume V. V_o stands for the equilibrium volume, B stands for the bulk modulus, and E_o is the total energy of the unit cell's ground state. B' is the pressure derivative of the bulk modulus. We determine the unit cell's volume value for which the total energy converges. These graphs show how the total energy varies for the unit cell volume and provide information about the material's bulk modulus and equilibrium volume. The order of relaxed unit cell volumes for $NaVH_3$, $NaTiH_3$, and $NaScH_3$ is as follows: $NaScH_3 > NaTiH_3 > NaVH_3$, with corresponding volumes of 62.40 Å^3, 52.30 Å^3, and 46.79 Å^3, respectively. This variation is primarily attributed to each compound's size of the M_T atom. In $NaScH_3$, the unit cell volume is the largest, mainly due to the relatively large size of the Sc atom. Conversely, in $NaVH_3$, the unit cell volume is smaller, primarily owing to the smaller size of the V atom. These unit cells' total energies follow a different order: $NaVH_3 > NaTiH_3 > NaScH_3$. It is concluded that these metal hydride perovskite crystal structures are considered energetically stable because the curve has been perfectly fitted using the Birch-Murnaghan equation of state to the calculated data points on the energy-volume curve [27–29].

3.2. Total Energies. Table 1 displays the computed lattice constants a (Å), volume V (Å^3), density (ρ), and total energies of the reactants and products of the reaction mentioned in Eq. (2). The formula for hydride perovskite formation for each compound is given below [30].

$$NaM_T + 1.5\,H_2 \longrightarrow NaM_tH_3 \quad (2)$$

The formation of NaM_TH_3 (M_T=Sc, Ti, V) was confirmed using the total energies. The difference in the energies of $E_{NaM_TH_3}$, E_{NaM_T}, and 3/2E(H_2) for M_T=Sc, Ti, and V was negative, which confirms the favorable hydride formation, which is thermodynamically stable. For instance, $NaScH_3$ has the lowest total energy $-2.64 \times 10^{+3}$ eV, indicating that it is the most stable, whereas NaSc $-2.58 \times 10^{+3}$ eV has a less negative value, which shows it is less stable than $NaScH_3$. Cwt% represents the gravimetric hydrogen storage capacity in Table 1. The sole purpose of this parameter is to access the compound for its potential use in hydrogen storage applications. If the calculated values of gravimetric hydrogen storage capacity are more than three, then the material is feasible for hydrogen storage. As shown in Table 1, the materials NaM_TH_3 (M_T=Sc, Ti, V) have storage capacities close to 4; hence, they are potential candidate for hydrogen storage applications. From the physical properties mentioned in Table 1, it can be seen that $NaScH_3$ has the largest value of lattice constant and, hence, the resulting unit cell volume, consequently, the lowest mass density.

3.3. Hydrogen Storage Properties. The volumetric hydrogen storage capacity (ρ (g.H_2/L)) is given by the following [31].

$$\rho_{\text{vol}} = \frac{N_H.m_H}{V(L).N_A} = \frac{5021.58}{\text{Vol.}\left(\overset{o}{A}\right)^3}. \quad (3)$$

Table 1: The calculated lattice constant ($a = b = c$ in Å), volume (V in Å^3), volumetric hydrogen storage capacity (ρ_{vol} in g.H_2/L), molar mass of transition metal, and gravimetric hydrogen storage capacity (Cwt% in wt%)for NaM_TH_3 (M_T=Sc, Ti, V).

Compounds	a_o	V	ρ_{vol} (g.H_2/L)	Cwt%
$NaScH_3$	3.97	62.40	80.47	4.26%
$NaTiH_3$	3.74	52.30	96.01	4.09%
$NaVH_3$	3.60	46.79	107.32	3.93%

The study calculates the NaM_TH_3 (M_T=Sc, Ti, V) hydride perovskites for hydrogen storage applications. The gravimetric storage capacity of perovskite structures was calculated using Eq. (3) and represented by Cwt%. Gravimetric capacity measures the quantity of stored hydrogen per unit mass of the studied hydride perovskite [32, 33].

$$\text{Cwt\%} = \left(\frac{(H/M)m_H}{m_{Host} + (H/M)m_H} \times 100\right)\%. \quad (4)$$

In this expression, m_H and m_{Host} serve for the molar mass of H_2 and NaM_T, whereas the H/M is the ratio of hydrogen atoms to transition metal atoms; in this case, it is three. The maximum storage capacity belongs to $NaScH_3$ with a 4.26% value. Remaining hydrides also have good storage capacities in the order Cwt%($NaScH_3$) > Cwt%($NaTiH_3$) > Cwt%($NaVH_3$), which follows the trend of unit cell volume. Figures 3 and 4 illustrate the gravimetric hydrogen storage capacity and volumetric hydrogen storage capacities of NaM_TH_3 (M_T=Sc, Ti, V) hydrides. Yet, it has the highest storage capacity values due to enough space available (due to the large lattice constant) within the unit cell for hydrogen to adsorb and desorb easily.

3.4. Phonon Dispersion and Phonon Density of State. Figure 5 shows the phonon dispersion and vibrational density of state graphs of studied hydrides along high symmetry lines in the first Brillouin zone. The unit cell contains a total of 5 atoms; therefore, 3 N modes of vibrations are present, including three acoustic modes and the remaining optical modes. The branches seem to be less than the vibrational modes due to the degeneration of phonons along high symmetry directions X to G and R to G. The energy difference between the low- and high-frequency phonon modes is 30.38, 34.45, and 33.05 THz for $NaScH_3$, $NaTiH_3$, and $NaVH_3$, respectively. $NaTiH_3$ shows the highest energy gap. This huge difference in the energy of phonons is due to the different masses of elements Na, Sc, Ti, V, and H. Overall, phonon dispersion and DOS curve represent convergent behavior, which depicts the dynamic stability of the studied hydride perovskites [34].

Figure 6 shows the projected phonon DOS of the investigated materials. Additionally, we conducted computations to determine the partial density of phonon states for NaM_TH_3 (M_T=Sc, Ti, V) hydride perovskites, where M_T represents Sc, Ti, or V. This analysis is aimed at explaining the atomic contributions within the overall density of phonon states of investigated material, as illustrated in

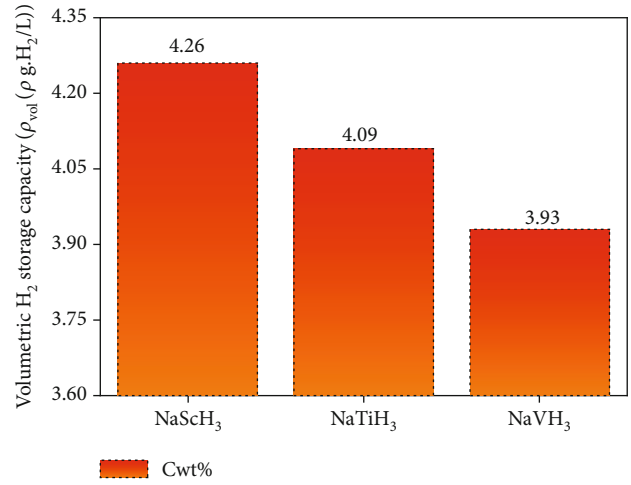

Figure 3: Calculated volumetric H_2 storage capacities of NaM_TH_3 (M_T=Sc, Ti, V).

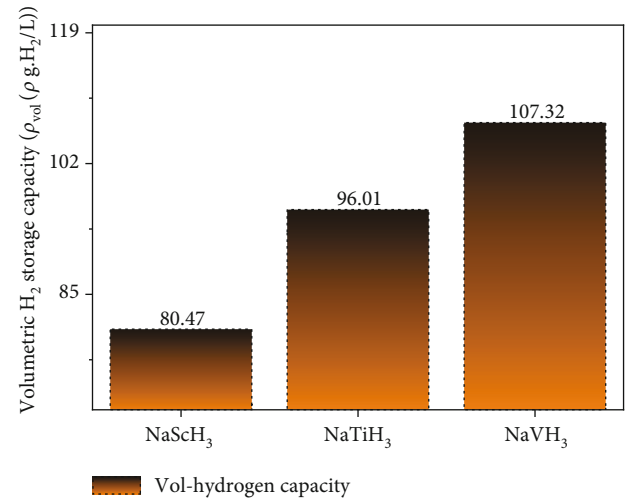

Figure 4: The calculated hydrogen storage capacities of NaM_TH_3 (M_T=Sc, Ti, V).

Figures 6(a)–6(c). The black lines represent the total density of phonon states of compounds, while the red line indicates the density of phonon states for the element Na. The green line illustrates the density of phonon states for transition elements M_T, where M_T can be Sc, Ti, or V, and the blue lines represent the density of phonon states for hydrogen atoms (H). In Figure 6(a), it is evident that the Na atom exhibits the highest peak in the density of phonon states in the low-frequency range, extending up to 4.35 THz. Conversely, the H atoms display moderate peaks in the high-frequency range spanning from 4.5 to 14.9 THz. Additionally, the transition atom Sc demonstrates minor peaks between 2.1 and 9.7 THz, but beyond this, its density of phonon states becomes negligible.

In Figure 6(b), in the low-frequency range, spanning up to 6.7 THz, the Na atom exhibits the most prominent peak in phonon state density. Conversely, H atoms display

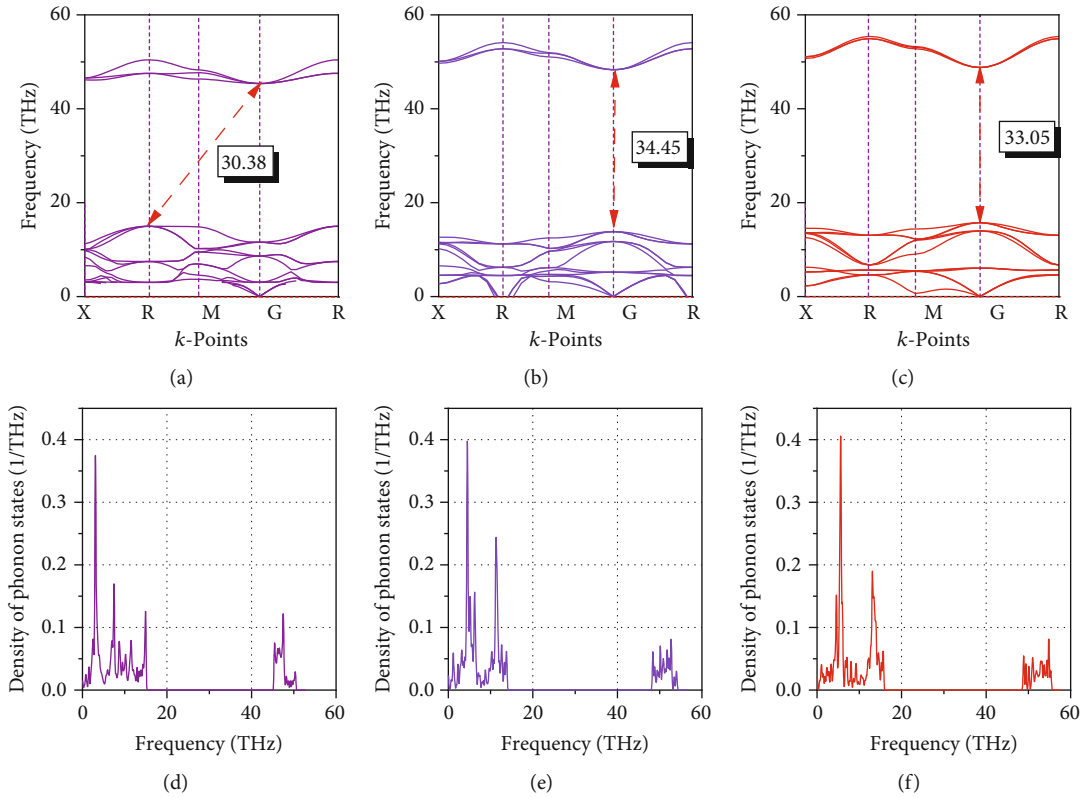

FIGURE 5: (a) Phonon dispersion of $NaScH_3$. (b) Phonon dispersion of $NaTiH_3$. (c) Phonon dispersion of $NaVH_3$. (d) Density of phonon states of $NaScH_3$. (e) Density of phonon states of $NaTiH_3$. (f) Density of phonon states of $NaVH_3$.

moderate peaks in the high-frequency range from 6.7 to 14 THz. Transition atoms Ti exhibit minor peaks below 6.8 THz, but their phonon state density becomes negligible beyond this frequency. A consistent pattern is observable in Figure 6(c). In the low-frequency range, spanning up to 6.4 THz, the Na atom exhibits the most prominent peak in phonon state density. Conversely, H atoms display moderate peaks in the high-frequency range from 6.4 to 15.9 THz. Transition atoms V also show minor peaks below 6.5 THz, but their phonon state density becomes negligible beyond this frequency.

3.5. Electronic Properties. To analyze the electronic properties of a material, its band structure and density of states were calculated. The band structures show charge carriers' quantum mechanical behavior and their metallic or nonmetallic behavior. Figure 7 depicts the electronic band structure of NaM_TH_3 (M_T=Sc, Ti, V) in the first Brillouin zone along the high symmetry directions. The band structure of all three hydrides shows the overlapping valence and conduction bands across the Fermi level, which is the characteristic of metallic material. The red-dotted line shows the Fermi level; energy levels above this line are called conduction bands, and lower ones are called valence bands.

The DOS $N_n(E)$ of n bands is defined as [35, 36]

$$N_n(E) = \int \frac{dk}{4\pi^3} \delta(E - E_n(k)). \tag{5}$$

$E_n(k)$ indicates the band's dispersion across the first Brillouin zone. By summarizing all the bands, the overall DOS is determined, which is given as [35]

$$N(E) = \sum N_n(E) = \sum \int \frac{dk}{4\pi^3} \delta(E - E_n(k)). \tag{6}$$

The DOS and PDOS were calculated using the GGA-PBE functional technique. Figure 8 shows the DOS (a, e, and i) and PDOS (b–d, f–h, and j–l) of the studied materials NaM_TH_3 (M_T=Sc, Ti, V). In TDOS, the density of state at the Fermi level is not zero, which shows the metallic nature of all hydride materials under investigation. PDOS shows the contribution of different atomic orbitals to the compound orbitals. These results are calculated from -5 eV to 10 eV to evaluate the role of individual elemental states in constructing TDOS of material. Sc, V, and Ti played the most crucial role in the TDOS near the fermi level, and further analysis revealed that they originate from d orbitals of transition metals. The bands towards the left of E_F are called valence bands, whereas the bands towards the right are called conduction bands [37].

In short, the metallic behavior and significant d orbital contributions of NaM_TH_3 (M_T=Sc, Ti, V) hydrides highlight their potential for potential as solid-state hydrogen storage materials.

3.5.1. Population Analysis and Electron Density Difference. The molecular characteristics and bonding, both inside and

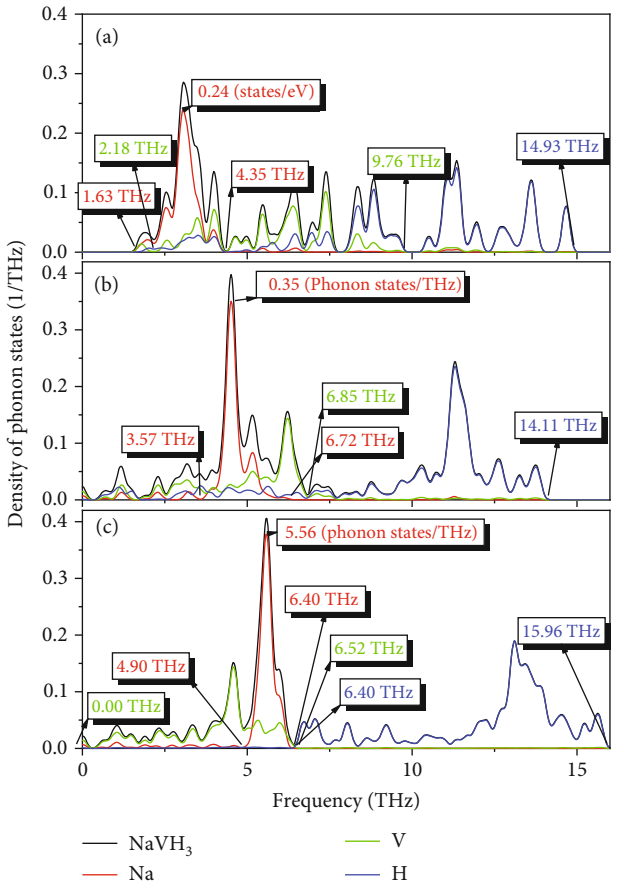

FIGURE 6: Partial density of phonon states of (a) $NaScH_3$, (b) $NaVH_3$, and (c) $NaTiH_3$.

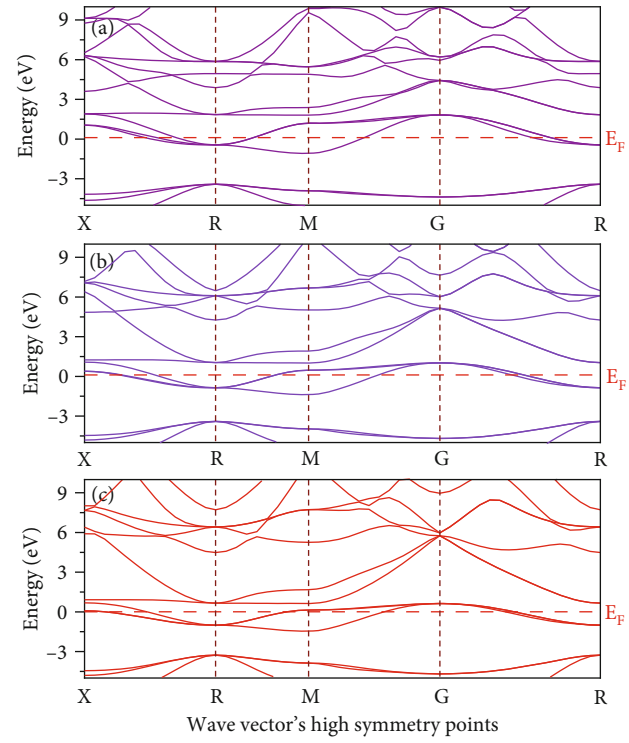

FIGURE 7: Electronic band structure of (a) $NaScH_3$, (b) $NaTiH_3$, and (c) $NaVH_3$.

between molecules, depend crucially on the distribution of atomic charge. The distribution of electronic charge density within atoms is better understood using population analysis. The Mulliken population and charge analysis was executed for the compounds $NaScH_3$, $NaTiH_3$, and $NaVH_3$. The Mulliken atomic population analysis represents a computational methodology employed for the examination of bonding characteristics, bond lengths, and electronic structures within both solids and molecules. The Mulliken analysis tells us how electrons are spread out in a material and can help us predict how it will react with hydrogen molecules.

Table 2 displays the atomic populations, charges, population averages, and average bond lengths of NaM_TH_3 (M_T=Sc, Ti, V). To evaluate the extent of covalent character in the given bonds, ionicity of population (f_n) was determined given by the following.

$$f_n = 1 - e^{(\lfloor P_C = P \rfloor)/P}. \quad (7)$$

A positive population value indicates the covalent bonding nature, while a negative value signifies the ionic bond formation. In our investigation, the bonds formed between a hydrogen atom (H) and transition metal atoms represented by M_T (where M_T = V, Ti, and Sc) are characterized by positive bond populations, indicative of covalent bonding. In contrast, the negative populations observed in the H-H and H-Na bonds imply an ionic nature for these bonds. The computational results indicate a positive charge for sodium (Na) and transition metals M_T (where M_T = V, Ti, and Sc), while hydrogen (H) is consistently found to carry a negative charge. The data demonstrates electron transfer occurring within the unit cell of $NaScH_3$, wherein both sodium and the transition metal element Sc transfer electrons to hydrogen. A similar trend is observed in the unit cells of $NaTiH_3$ and $NaVH_3$, where electrons are also transferred from sodium and the respective transition metals (Ti and V) to hydrogen, forming strong bonds [13]. Furthermore, in these compounds ($NaScH_3$, $NaTiH_3$, and $NaVH_3$), the bond length exhibits the following trend: H-Sc > H-Ti > H-V, with corresponding values of 1.98 Å, 1.87 Å, and 1.80 Å, respectively. Although all of these transition metal atoms (Sc, Ti, and V) make covalent bonds with hydrogen, the H-Sc bond length is the largest. Therefore, in this study, $NaScH_3$ is found to be the best material for hydrogen storage among NaM_TH_3 (M_T=Sc, Ti, V) hydrides, due to its favorable properties. The population analysis and electron density difference, along with charge density distribution, are vital in exploring the hydrogen storage capacities of lead-free perovskite NaM_TH_3 as an efficient solid-state hydrogen storage material [38, 39].

3.6. Charge Density Distribution. To better understand the nature of bonds in our compounds and the distribution of charge around the atoms, we examined electronic charge

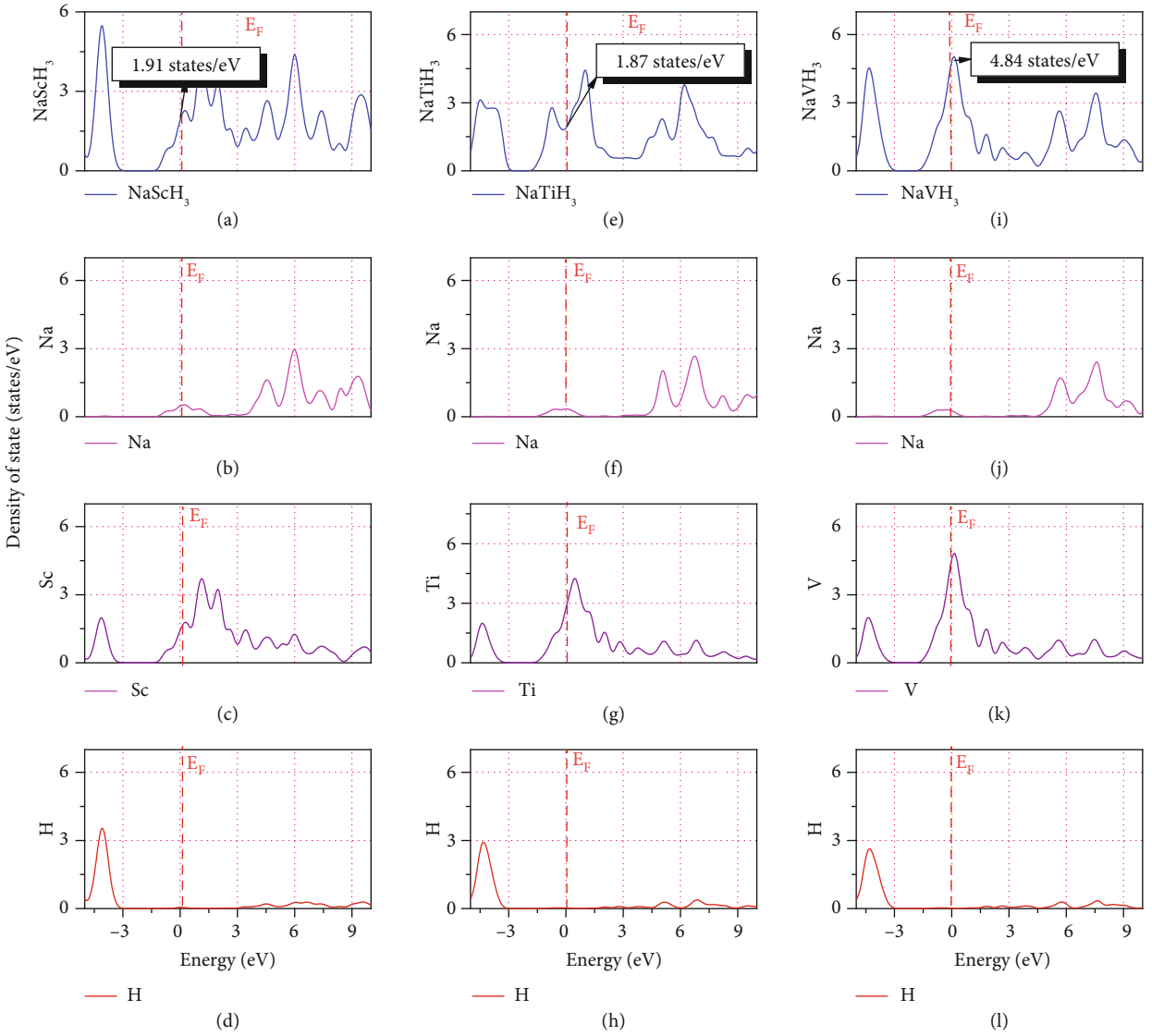

Figure 8: TDOS of (a) $NaScH_3$, (b) Na, (c) Sc, (d) H, (e) $NaTiH_3$, (f) Na, (g) Ti, (h) H, (i) $NaVH_3$, (j) Na, (k) V, and (l) H.

Table 2: The calculated values of the Mulliken population and charge analysis for NaM_TH_3 (M_T=V, Ti, Sc) hydride perovskites.

Compound	Species	*s*	*p*	*d*	*f*	Total	Charge	Bond	Population	Bond length (Å)
$NaScH_3$	Na	2.13	6.00	0	0	8.14	0.86	H-Na	-0.10	2.80
	Sc	2.34	6.76	1.63	0	10.73	0.27	H-Sc	0.70	1.98
	H	1.38	0	0	0	1.38	-0.38	H-H	-0.05	2.80
$NaTiH_3$	Na	2.09	5.95	0	0	8.03	0.97	H-Na	-0.22	2.64
	Ti	2.39	6.82	2.71	0	11.92	0.08	H-Ti	0.79	1.87
	H	1.35	0	0	0	1.35	-0.35	H-H	-0.06	2.64
$NaVH_3$	Na	2.08	5.93	0	0	8.02	0.98	H-Na	-0.26	2.55
	V	2.42	6.76	3.82	0	13	0	H-V	0.81	1.80
	H	1.33	0	0	0	1.33	-0.33	H-H	-0.05	2.55

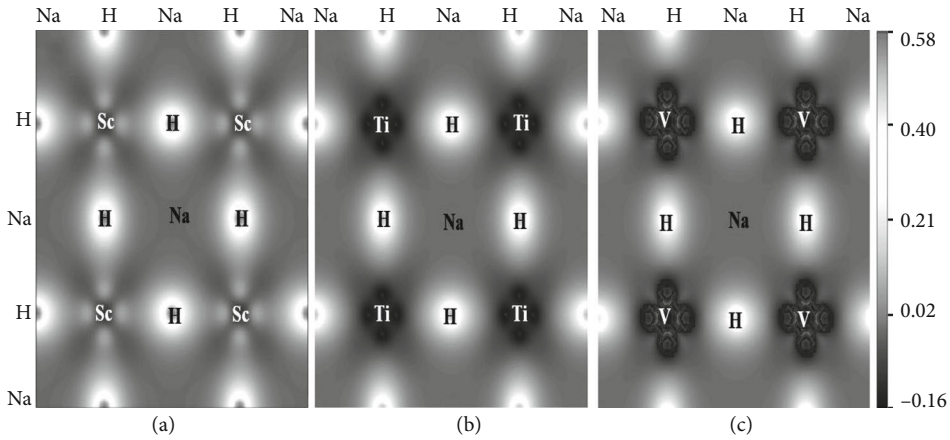

Figure 9: Electronic charge density of (a) $NaScH_3$, (b) $NaTiH_3$, and (c) $NaVH_3$.

density mappings. Figure 9 illustrates the findings from the investigation of the charge density distribution in NaM_TH_3 compounds, where M_T represents V, Ti, and Sc, within the (001) crystallographic plane. The graph's right side features a color scale indicating the charge density, with light grey indicating high density and dark grey representing low density. This implies the formation of strong covalent bonds between Na and elements such as V, Ti, and Sc, denoted as Na-M_T. Conversely, H-H and H-Na bonds exhibit ionic interactions, affirming the findings indicated by population analysis. The characterization of bond nature and bond length between transition metals M_T (V, Ti, Sc) and hydrogen atom H is of significant importance. Based on the information presented in Figure 9, it can be affirmed that the bonds between H and V, Ti, and Sc are covalent in nature, exhibiting considerable distortion and significant electron cloud overlap around these atoms. The bond lengths between a hydrogen atom (H) and transition metals (X) such as V, Ti, and Sc exhibit the following trend: H—Sc > H—Ti > H–V, with corresponding values of 1.98, 1.87, and 1.80, respectively.

3.7. Mechanical Properties. The crystal energy, equilibrium volume, and the strain-dependent matrix having second-order elastic constants (C_{ij}) are used to provide insight into the elastic behavior of the NaM_TH_3 (M_T=Sc, Ti, V) hydride perovskite. Mechanical characteristics are interlinked with the elastic constants denoted as C_{ij}. The elastic constants of a material can define how it behaves under applied stress from the outside and offer important information about its bonding properties and structural stability [40]. For the compounds $NaVH_3$, $NaTiH_3$, and $NaScH_3$, the computed values of the elastic constants C_{11}, C_{12}, and C_{44} for cubic single-crystalline structures are presented in Table 3. These values can be utilized for the evaluation of the mechanical stability of these compounds. The Born-Huang lattice dynamical theory has the ability to assess the mechanical stability of compounds. Given the cubic arrangement exhibited by these compounds, it is imperative to apply the Born stability criteria for the purpose

Table 3: The calculated elastic constants (C_{ij}) and C_p for NaM_TH_3 (M_T=Sc, Ti, V).

Compound	C_{11}	C_{12}	C_{44}	$C_p = C_{12} - C_{44}$
$NaScH_3$	129.85	38.20	50.98	-12.77
$NaTiH_3$	118.25	30.15	38.74	-8.60
$NaVH_3$	91.66	22.07	25.07	-2.99

of evaluating their stability. The requisite conditions are as follows [41]:

$$C_{11} - C_{12} > 0, \tag{8}$$

$$C_{11} + 2C_{12} > 0, \tag{9}$$

$$C_{44} > 0. \tag{10}$$

Analyzing the data by Equations (3)–(5) presented in Table 3, it is evident that all three compounds satisfy the established criteria for mechanical stability. Consequently, the structures of $NaVH_3$, $NaTiH_3$, and $NaScH_3$ demonstrate mechanical stability. The Cauchy pressure, C_p, can be computed by deducting the C_{44} value from C_{12}.

$$C_p = C_{12} - C_{44}. \tag{11}$$

The C_p sign of the compound can be used to identify whether it would behave brittle or ductile. While a negative C_p shows brittle behavior, a positive C_p indicates ductile behavior. As in our case, all the studied compounds show brittle behavior as the C_p for all compounds is negative. Furthermore, the utilization of elastic constants extends to the derivation of additional mechanical properties of a material, including the shear modulus, Young's modulus, and Poisson's ratio [42]. Consequently, extensive inquiries have been conducted into the elastic constants of compounds involving NaM_TH_3 (M_T=Sc, Ti, V) hydride perovskites. The bulk modulus (B) Eq. (10), shear modulus (G) Eq. (12), Young modulus (E) Eq. (13), and Poisson's ratio (v) Eq. (14) were assessed utilizing the Voigt-Reuss-Hill

(VRH) approximations. The Voigt approximation establishes an upper limit for the modulus, whereas the Reuss approximation sets a lower limit. In comparison, the Hill approximation offers enhanced accuracy. The data presented in Table 4 was derived employing the Hill approximation method.

$$B = B_R = B_V, \tag{12}$$

$$G = \frac{1}{2}(G_v + G_R), \tag{13}$$

$$E = \frac{9GB}{(G + 3B)}, \tag{14}$$

$$\nu = \frac{3B - 2G}{6B + 2G}. \tag{15}$$

Table 3 shows the values of elastic constants of investigated hydrides. $NaScH_3$ has the lowest value of Cp. $NaScH_3$ expresses the strongest contraction under pressure with a Cauchy's pressure of -12.77, followed by $NaTiH_3$ (-8.60) and $NaVH_3$ (-2.99), indicating their decreasing response to contract under compression. The calculated values of bulk modulus are also mentioned in Table 4, which represents the ratio of a small increase in pressure to the decrease in volume (compression), or its resistance to compression; the highest value corresponds to $NaVH_3$. The shear modulus (G) represents the ratio of shear stress to shear strain; the highest value of G belongs to $NaVH_3$. Young's modulus reflects the degree of the stiffness of a solid material, defined as the ratio of stress to strain along the same axis. $NaVH_3$ has the highest Young's modulus of 118.49, followed by $NaTiH_3$ with 99.61 and $NaScH_3$ with 70.86, making $NaVH_3$ comparatively the stiffest material.

Another important parameter to determine the bonding strength of the material is Poisson's ratio. It is a measure of compression or expansion of studied perovskite hydride in the normal direction and is related to the bond type of the material. The ionic and covalent bonding criterion is ν greater than 0.25 and $\nu = 0.1$, respectively. The respective Poisson ratios were calculated for investigated materials and can be found in Table 4. The results show that $NaVH_3$ has more covalent character, $NaTiH_3$ has a balanced covalent and ionic character, and $NaScH_3$ has more ionic character based on their Poisson ratios. The B/G (Pugh's ratio) was measured to predict the ductile or brittleness of the material. For ductile materials, the B/G ratio is greater than 1.75. The calculated values in Table 4 confirm that the studied materials are brittle. The elastic anisotropy index (A) values were calculated using the following [43].

$$A_{i(i=1,2,3)} = \frac{2C_{44}}{C_{11} - C_{12}}. \tag{16}$$

If the material has isotropic elastic behavior, the anisotropic factor value will not be 1 (one). Therefore, all compounds exhibit elastic anisotropic behavior percentage anisotropy factor known as B_k and G_k using Eq. (17) [43]. These parameters indicate the level of elastic anisotropy in the bulk and shear modulus. For isotropic medium, the measured values of these parameters are zero; conversely, the medium is anisotropic.

Table 4: The calculated anisotropic factor (AU), bulk modulus (B in GPa), shear modulus (G in GPa), Young modulus (E in GPa), B/G, G/B, Poisson ratio (ν), and Vickers hardness (H_v in GPa) for NaM_TH_3 (M_T=Sc, Ti, V) hydrides.

Compound	A^U	B	G	E	B/G	G/B	ν	H_v
$NaVH_3$	0.01	68.76	48.85	118.49	1.41	0.71	0.21	9.79
$NaTiH_3$	0.02	59.52	40.78	99.61	1.46	0.69	0.22	8.27
$NaScH_3$	0.13	45.27	28.59	70.86	1.58	0.63	0.24	5.86

$$B_k = \frac{B_V - B_R}{B_V + B_R} \text{ and } G_k = \frac{G_V - G_R}{G_V + G_R}. \tag{17}$$

The result mentioned in Table 3 indicates that all three hydrides are isotropic; only $NaScH_3$ shows a small value of 1.2% of anisotropy in shear modulus. The Vickers hardness of a material is given by

$$H_v = 2\left(\left(\frac{G}{B}\right)^2 G\right)^{0.585} - 3. \tag{18}$$

Among the studied materials, $NaVH_3$ exhibits the highest HV value, indicating that it is a relatively hard material. Conversely, $NaScH_3$ has the lowest hardness due to its minimal HV value. Based on the hardness test, these compounds are soft materials because their calculated hardness values fall below the hardness threshold of 40 GPa.

The hydrogen adsorption and desorption processes are governed by thermal energy; therefore, it is essential to investigate the thermodynamic properties of the material.

The Debye temperature is used as an indicator to investigate the thermal conductivity and interatomic force. This temperature is interrelated to the elastic vibrations of the crystal and depends on the material's average sound velocity (V_m). The Debye temperature of crystals under investigation is calculated by Voigt-Reuss approximation as [44]

$$\theta_{Deb} = \frac{h}{k_B}\left[\frac{3n}{4\pi}\left(\frac{N_A\rho}{M}\right)\right]^{1/3} \nu_m. \tag{19}$$

In this context, h, k_B., N_A, ρ, M, and n are, respectively, Planck's constant (1.381×10^{-23}J/K), Boltzmann constant (6.626×10^{-34}Js), Avogadro's number (6.022×10^{23}), density of crystal, molar mass, and number of atoms per unit cell, and V_m represents the average sound velocity.

The average sound velocities for $NaScH_3$, $NaTiH_3$, and $NaVH_3$ cubic crystals were around 4302 m/s, 4610 m/s, and 4673 m/s, respectively. These sound velocities are related to Debye temperature, reflecting the material's stiffness properties. For cubic crystals NaM_TH_3 (M_T=Sc, Ti, V), the respective Debye temperatures were calculated as 552.2 K, 626.3 K, and 660.1 K. The results depict that the

stiffness of these materials follows the order $NaScH_3 < NaTiH_3 < NaVH_3$. Notably, the highest value of Debye temperature belongs to $NaVH_3$, which indicates the highest conductivity value.

Another important parameter is the melting temperature of these cubic crystals calculated by using the formula given as [44]

$$T_{\text{mel}}(\text{K}) = (5.911 \times C_{12} + 553)\text{GPa} \pm 300\text{K}. \quad (20)$$

The computed melting temperatures for hydrides NaM_TH_3 (M_T=Sc, Ti, V) were found to be 683.479 K, 731.214 K, and 778.858 K, respectively. Results show that the melting temperature of these perovskites increases in the order of $NaScH_3 < NaTiH_3 < NaVH_3$. $NaScH_3$ has the lowest melting temperature, whereas $NaVH_3$ has the highest melting temperature. The Debye temperature, average sound velocity, and other such quantities are mentioned in Table 5.

The mechanical properties, including elastic behavior and stability, of NaM_TH_3 (MT=Sc, Ti, V) hydrides, as revealed by the analysis, underscore their potential as solid-state hydrogen storage materials, aligning with the study's objective.

3.8. Thermodynamical Properties. To investigate the thermal stability of the NaM_TH_3 (M_T=Sc, Ti, V) materials, quasiharmonic approximation was implemented using CASTEP code [45]. This study was performed in the absence of any external pressure. The collective effect of heat absorption, elastic vibration (phonon), and electrons can be elaborated using the specific heat capacity of materials [46]. The specific heat capacity at constant volume is equivalent to the amount of heat absorbed by the material as a result of a one-degree Kelvin change in temperature. Figure 10 shows the enthalpy, free energy, entropy, and specific heat capacities at constant volume of hydride materials under investigation. The specific heat capacities of hydride materials follow the order $NaTiH_3 > NaVH_3 > NaScH_3$. Notably, the C_v curves are steepest at the start, but after 200 K, the slope decreases. This may be due to the harmonic effects and coincides with the prediction of the Dulong-Petit law ($C_v = 3R$ for any solid material). Figures 10(a)–10(f) represents the thermodynamics of NaM_TH_3 (M_T=Sc, Ti, V) materials for the temperature range 0 K to 1000 K. In Figures 10(a), 10(c), and 10(e), before 110 K, the values of enthalpy (H), temperature times entropy ($T * S$), and Helmholtz free energy (F_{Helm}) were zero—afterward, the free energy decreases, whereas the enthalpy and entropy increase. Enthalpy itself is calculated by taking the sum of internal energy and the product of pressure volume ($H = E + PV$). An enthalpy of 0.89 eV is noted for $NaTiH_3$ and $NaVH_3$, which is greater than the corresponding values of enthalpy for $NaScH_3$ at 1000 K. To evaluate the thermal stability of these hydrides, free energies were noted. It is well established that negative values of free energies ensure the thermodynamic stability of a material. The maximum values of free energies of hydrides NaM_TH_3 (M_T=Sc, Ti, V) are -1.28 eV, -1.39 eV, and -131 eV, respectively, at 1000 K; these negative values show the thermodynamic stability of hydride under investigation. The entropy of the system represents the thermal energy of a system. From the graphs, the entropy or thermal energy of the system was zero at zero Kelvin. Still, after 110 K, the value started to increase due to an increase in thermal agitation of crystal atoms with the rise of temperature.

Table 5: The calculated values of density (ρ in kg/m^3), molar mass (M in kg/mol), average sound velocity (V_m in m/s), Debye temperature (θ_D in K), and melting temperature (T_m in K) for NaM_TH_3 (M_T=Sc, Ti, V) hydride perovskites.

Compound	ρ	M	V_m	θ_D	T_m
$NaVH_3$	1888.556	0.0709695	4302.441	552.217	683.479
$NaTiH_3$	2331.878	0.0738806	4609.879	626.311	731.214
$NaScH_3$	2731.089	0.0769551	4672.759	660.158	778.858

In Figures 10(b), 10(d), and 10(f), the heat capacity of NaM_TH_3 (M_T=Sc, Ti, V) and constituent elements are shown; graphs show that hydrogen has the minimum value of heat capacity at Dulong-Petit limit, followed by transition metal and sodium, and the highest value of heat capacity is achieved by perovskite hydrides.

For perovskite hydride material under investigation, ZPE represents the minimum energy at absolute zero temperature, E represents the system's internal energy, F shows the material's thermodynamic stability, and S reflects the degree of disorder.

From calculation of these thermodynamic properties, it can be inferred that the material properties of $NaScH_3$, $NaVH_3$, and $NaTiH_3$ are unique at a temperature of 298 K. $NaScH_3$ has the minimum value of internal energy (0.61 eV), Helmholtz free energy (0.30 eV), and heat capacity at constant volume (81.15 J/mol/K), but the maximum value of entropy (100.19 J/mol/K), whereas $NaVH_3$ has the highest zero-point energy (0.54 eV) and internal energy (0.69 eV), but the lowest entropy (91.38 J/mol/K) and average value of heat capacity at constant volume (83.37 J/mol/K). Additionally, $NaTiH_3$ has an average value for all properties except the heat capacity (87.47 J/mol/K) which is highest among the three materials. To assess thermodynamic stability, we identified the lowest Helmholtz free energy (0.3 eV) value, which corresponds to $NaScH_3$. Hence, $NaScH_3$ has the highest thermodynamic stability among the three materials at a temperature of 298 K.

Figure 11 shows the plots of variation of Debye temperature along with temperature for the respective hydrides. The highest values belong to $NaScH_3$, which represents its comparatively high conductivity. The results show that $NaScH_3$ is thermodynamically stable and suitable for hydrogen storage. Out of all three hydrides, the heat capacity of $NaScH_3$ is the lowest, but the conductivity (Debye temperature) is high; therefore, it can conduct heat supplied for desorption. From Figure 11, it is obvious that the Debye temperature of $NaScH_3$ is the highest, and $NaVH_3$ is the lowest.

The mechanical and thermodynamic property analysis confirms the potential of lead-free perovskite NaM_TH_3

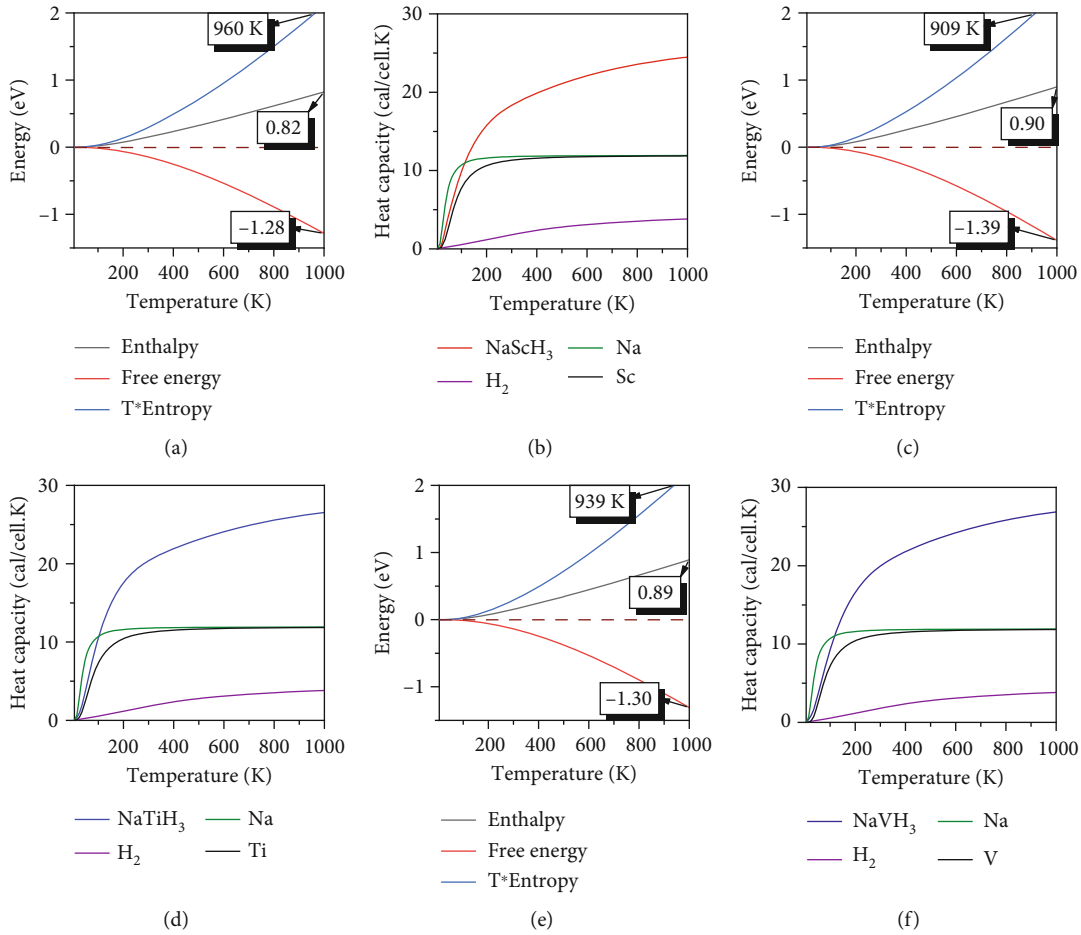

Figure 10: Thermodynamic properties of (a, b) $NaScH_3$, (c, d) $NaTiH_3$, and (e, f) $NaVH_3$.

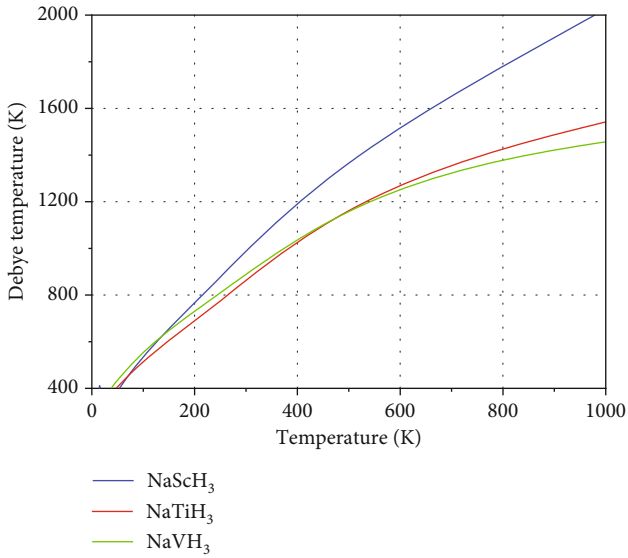

Figure 11: The calculated graphs of Debye temperature of NaM_TH_3 (M_T=Sc, Ti, V).

(M_T=Sc, Ti, V) as a solid-state hydrogen storage material, aligning with the focus on hydrogen storage capacity.

4. Conclusion

NaM_TH_3 (M_T=Sc, Ti, V) hydride perovskites were investigated using DFT. Our results showed that the gravimetric hydrogen storage capacities of these hydrides $NaScH_3$, $NaVH_3$, and $NaTiH_3$ are 4.26 wt%, 4.09 wt%, and 3.83 wt%, respectively. As per Born's criterion, the studied perovskites express mechanical stability. The anisotropy index revealed the isotropic behavior for shear and bulk moduli. The Vickers hardness results showed that these perovskites are soft materials. The Poisson ratios revealed $NaVH_3$ being more covalent, $NaTiH_3$ being balanced, and $NaScH_3$ being more ionic. Electronic band structure and DOS analysis revealed the metallic nature, further supporting their potential for hydrogen storage. Population analysis revealed appropriate bond lengths, boosting the stable perovskite structure role as hydrogen storage medium. The dynamic stability of these hydrides was obvious from the absence of imaginary frequencies in phonon dispersion curves. As temperature rises, specific heat, entropy, and Debye temperature increase, while free energy turns negative. $NaScH_3$ shows exceptional

properties among studied hydrides, indicating its capability as a hydrogen storage material.

Data Availability

No data was used for this work.

Ethical Approval

All authors confirm that the submitted work is original, has not been published elsewhere, and adheres to ethical guidelines.

Consent

All authors have seen and agreed to publish the final version of the manuscript. Authors typically transfer the copyright of their research article to the journal's publisher. Authors grant the journal the right to publish their work in various formats, including print and electronic versions.

Conflicts of Interest

The authors declare that they have no competing interests related to the research, authorship, or publication of this article. No financial, professional, personal, or other associations that could be perceived as influencing the research or its presentation in this manuscript exist.

Authors' Contributions

Conceptualization, writing of the original draft, and supervision were carried out by Zia ur Rehman. Data curation and writing, reviewing, and editing the manuscript were performed by Muhammad Awais Rehman. Investigation, resources, and data collection are contributed by Suliman Yousef Alomar. Methodology, validation, and visualization were responsible of Bushra Rehman. Investigation was carried out by Muhammad Awais. Writing, reviewing, and editing the manuscript were performed by Mahnoor Amjad. Data curation and resources were contributed by Surajudeen Sikiru. Methodology and formal analysis were performed by Esraa Mousa Ali. Revising the manuscript was done by Abu Hamad.

Acknowledgments

The authors would like to thank the Researchers Supporting Project Number (RSP2024R35), King Saud University, Riyadh, Saudi Arabia.

References

[1] A. Züttel, A. Remhof, A. Borgschulte, and O. Friedrichs, "Hydrogen: the future energy carrier," *Philosophical Transactions of the Royal Society A: Mathematical, Physical and Engineering Sciences*, vol. 368, no. 1923, pp. 3329–3342, 2010.

[2] K. L. Lim, H. Kazemian, Z. Yaakob, and W. R. W. Daud, "Solid-state materials and methods for hydrogen storage: a critical review," *Chemical Engineering & Technology: Industrial Chemistry-Plant Equipment-Process Engineering-Biotechnology*, vol. 33, no. 2, pp. 213–226, 2010.

[3] H. Cheng, C. Liang, A. C. Cooper, X. Sha, and G. P. Pez, "Hydrogen spillover in the context of hydrogen storage using solid-state materials," *Energy & Environmental Science*, vol. 1, no. 3, pp. 338–354, 2008.

[4] S.-P. Chan, G. Chen, X. G. Gong, and Z.-F. Liu, "Chemisorption of hydrogen molecules on carbon nanotubes under high pressure," *Physical Review Letters*, vol. 87, no. 20, article 205502, 2001.

[5] X. Zhang, Y. Tang, F. Zhang, and C.-S. Lee, "A novel aluminum–graphite dual-ion battery," *Advanced Energy Materials*, vol. 6, no. 11, article 1502588, 2016.

[6] T. Sato, D. Noréus, H. Takeshita, and U. Häussermann, "Hydrides with the perovskite structure: general bonding and stability considerations and the new representative CaNiH3," *Journal of Solid State Chemistry*, vol. 178, no. 11, pp. 3381–3388, 2005.

[7] N. A. Shahed, M. Nishat, S. Khanom, M. K. Hossain, M. A. Hossain, and F. Ahmed, "Effect of oxygen deficiency on optical and magnetic properties of Ba2MMoO6 (M= Cr, Mn, Fe): a first-principles study," *Computational Condensed Matter*, vol. 23, article e00464, 2020.

[8] M. Wang, C. Jiang, S. Zhang, X. Song, Y. Tang, and H.-M. Cheng, "Reversible calcium alloying enables a practical room-temperature rechargeable calcium-ion battery with a high discharge voltage," *Nature Chemistry*, vol. 10, no. 6, pp. 667–672, 2018.

[9] M. N. Islam, M. A. Hadi, and J. Podder, "Influence of Ni doping in a lead-halide and a lead-free halide perovskites for optoelectronic applications," *AIP Advances*, vol. 9, no. 12, 2019.

[10] A. Gencer and G. Surucu, "Investigation of structural, electronic and lattice dynamical properties of XNiH (X = Li, Na and K) perovskite type hydrides and their hydrogen storage applications," *International Journal of Hydrogen Energy*, vol. 44, no. 29, pp. 15173–15182, 2019.

[11] S. Mu, Q. Liu, P. Kidkhunthod, X. Zhou, W. Wang, and Y. Tang, "Molecular grafting towards high-fraction active nanodots implanted in N-doped carbon for sodium dual-ion batteries," *National Science Review*, vol. 8, no. 7, article nwaa178, 2020.

[12] X. Qi, F. Yu, Z. Meng, Z. Sun, N. Zhang, and Z. Guo, "Preliminary design of the suppressive containment system based on HPR1000," *Nuclear Engineering and Design*, vol. 415, article 112743, 2023.

[13] Z. Huang, P. Luo, S. Jia, H. Zheng, and Z. Lyu, "A sulfur-doped carbon-enhanced Na3V2 (PO4) 3 nanocomposite for sodium-ion storage," *Journal of Physics and Chemistry of Solids*, vol. 167, article 110746, 2022.

[14] J. Fatima, M. B. Tahir, M. A. Rehman et al., "Structural, optical and electronic properties of novel 2D carbides and nitrides MXene based Materials: a DFT study," *Optical and Quantum Electronics*, vol. 55, no. 7, p. 576, 2023.

[15] Z. Huang, P. Luo, Q. Wu, and H. Zheng, "Constructing one-dimensional mesoporous carbon nanofibers loaded with NaTi2 (PO4) 3 nanodots as novel anodes for sodium energy storage," *Journal of Physics and Chemistry of Solids*, vol. 161, article 110479, 2022.

[16] Y. Bouhadda, M. Bououdina, N. Fenineche, and Y. Boudouma, "Elastic properties of perovskite-type hydride NaMgH3 for hydrogen storage," *International Journal of Hydrogen Energy*, vol. 38, no. 3, pp. 1484–1489, 2013.

[17] G. Surucu, A. Candan, A. Gencer, and M. Isik, "First-principle investigation for the hydrogen storage properties of NaXH3 (X= Mn, Fe, Co) perovskite type hydrides," *International Journal of Hydrogen Energy*, vol. 44, no. 57, pp. 30218–30225, 2019.

[18] X.-F. Chen, "Periodic density functional theory (PDFT) simulating crystal structures with microporous CHA framework: an accuracy and efficiency study," *Inorganics*, vol. 11, no. 5, p. 215, 2023.

[19] X. Chen and Y. Tie, "Simulating crystal structure, acidity, proton distribution, and IR spectra of acid zeolite HSAPO-34: a high accuracy study," *Molecules*, vol. 28, no. 24, p. 8087, 2023.

[20] J. U. Rehman, M. A. Rehman, M. B. Tahir et al., "Electronic and optical properties of nitrogen and sulfur doped strontium titanate as efficient photocatalyst for water splitting: a DFT study," *International Journal of Hydrogen Energy*, vol. 47, no. 3, pp. 1605–1612, 2022.

[21] Z. ur Rehman, M. A. Rehman, H. Chaudhry, and M. Awais, "Ab initio insight into the structural, vibrational, electronic, optical, magnetic, and thermal properties of lead-free perovskite Cs3Sb2Cl9 for solar cell application," *Journal of Physics and Chemistry of Solids*, vol. 182, article 111548, 2023.

[22] M. A. Rehman, J. u. Rehman, and M. B. Tahir, "Density functional theory study of structural, electronic, optical, mechanical, and thermodynamic properties of halide double perovskites Cs2AgBiX6 (X= Cl, Br, I) for photovoltaic applications," *Journal of Physics and Chemistry of Solids*, vol. 181, article 111443, 2023.

[23] S. Ye, J. Zhu, S. Zhu et al., "Design strategies for perovskite-type high-entropy oxides with applications in optics," *ACS Applied Materials & Interfaces*, vol. 15, no. 40, pp. 47475–47486, 2023.

[24] J. U. Rehman, M. A. Rehman, M. Usman et al., "A DFT study to investigate structural, electronic, optical, mechanical and magnetic properties of NaGeBr3 for photovoltaic and optoelectronic applications," *Emergent Materials*, vol. 6, no. 2, pp. 699–709, 2023.

[25] J. U. Rehman, M. Usman, S. Amjid et al., "First-principles calculations to investigate structural, electronics, optical and elastic properties of Sn-based inorganic halide-perovskites CsSnX3 (X= I, Br, Cl) for solar cell applications," *Computational and Theoretical Chemistry*, vol. 1209, article 113624, 2022.

[26] J. Chen, Z. Zhang, and L. Hao, "Structure design and properties investigation of Bi2O2Se/graphene van der Waals heterojunction from first-principles study," *Surfaces and Interfaces*, vol. 33, article 102289, 2022.

[27] Z. Li, H. Li, X. Zhu et al., "Directly printed embedded metal mesh for flexible transparent electrode via liquid substrate electric-field-driven jet," *Advanced Science*, vol. 9, no. 14, article e2105331, 2022.

[28] H. Li, Z. Li, N. Li et al., "3D printed high performance silver mesh for transparent glass heaters through liquid sacrificial substrate electric-field-driven jet," *Small*, vol. 18, no. 17, article 2107811, 2022.

[29] H. Zhang, X. Zhu, Y. Tai et al., "Recent advances in nanofiber-based flexible transparent electrodes," *International Journal of Extreme Manufacturing*, vol. 5, no. 3, article 032005, 2023.

[30] P. Schouwink, M. B. Ley, A. Tissot et al., "Structure and properties of complex hydride perovskite materials," *Nature Communications*, vol. 5, no. 1, p. 5706, 2014.

[31] G. Cipriani, V. Di Dio, F. Genduso et al., "Perspective on hydrogen energy carrier and its automotive applications," *International Journal of Hydrogen Energy*, vol. 39, no. 16, pp. 8482–8494, 2014.

[32] Q. Huang, S. Jiang, Y. Wang et al., "Highly active and durable triple conducting composite air electrode for low-temperature protonic ceramic fuel cells," *Nano Research*, vol. 16, no. 7, pp. 9280–9288, 2023.

[33] A. Mera and M. A. Rehman, "First-principles investigation for the hydrogen storage properties of AeSiH3 (Ae= Li, K, Na, Mg) perovskite-type hydrides," *International Journal of Hydrogen Energy*, vol. 50, pp. 1435–1447, 2024.

[34] C. Lu, R. Ren, Z. Zhu et al., "BaCo0.4Fe0.4Nb0.1Sc0.1O3-δ perovskite oxide with super hydration capacity for a high-activity proton ceramic electrolytic cell oxygen electrode," *Chemical Engineering Journal*, vol. 472, article 144878, 2023.

[35] J. U. Rehman, M. A. Rehman, M. Usman et al., "First-principles calculations to investigate structural, electronics, optical and mechanical properties of $LaRu_2P_2$ compound for superconducting application," *Molecular Simulation*, vol. 49, no. 1, pp. 76–84, 2023.

[36] H. Wang, Z. Huang, X. Zeng, J. Li, Y. Zhang, and H. Qinghua, "Enhanced anticarbonization and electrical performance of epoxy resin via densified spherical boron nitride networks," *ACS Applied Electronic Materials*, vol. 5, no. 7, pp. 3726–3732, 2023.

[37] X. Feng, L. Sun, W. Wang, Y. Zhao, and J.-W. Shi, "Construction of CdS@ ZnO core–shell nanorod arrays by atomic layer deposition for efficient photoelectrochemical H2 evolution," *Separation and Purification Technology*, vol. 324, article 124520, 2023.

[38] Z. Sheng, M. Cheng, and J.-P. Wang, "Multi-wave effects on stability and performance in rotating detonation combustors," *Physics of Fluids*, vol. 35, no. 7, 2023.

[39] T. Wei, Y. Zhou, S. Cheng et al., "An intermittent lithium deposition model based on CuMn-bimetallic MOF derivatives for composite lithium anode with ultrahigh areal capacity and current densities," *Nano Research*, pp. 1–7, 2023.

[40] A. A. Mousa, S. M. Al Azar, S. SâadEssaoud et al., "Structural, elastic, electronic, magnetic, and thermoelectric characteristics of MgEu2X4(X = S, Se) spinel compounds: ab-initio calculations," *Physica Status Solidi (b)*, vol. 259, no. 10, article 2200191, 2022.

[41] M. A. Rehman, J. ur Rehman, and M. B. Tahir, "A DFT study of structural, electronic, optical, mechanical, thermoelectric, and magnetic properties of Pb-halide perovskites LiPbX3 (X= Cl, Br, and I) for photovoltaic applications," *Computational and Theoretical Chemistry*, vol. 1223, article 114085, 2023.

[42] G. Surucu, A. Gencer, A. Candan, H. H. Gullu, and M. Isik, "CaXH3 (X= Mn, Fe, Co) perovskite-type hydrides for hydrogen storage applications," *International Journal of Energy Research*, vol. 44, no. 3, pp. 2345–2354, 2020.

[43] Y. Tian, G. Jia, and W. Ping, "First-principles study on the structural, elastic and thermodynamic properties of binary Pd-Sn compounds," *Journal of Electronic Materials*, vol. 52, no. 3, pp. 1875–1887, 2023.

[44] A. Siddique, A. Khalil, B. S. Almutairi et al., "Structural, electronic, mechanical and dynamical stability properties of LiAH3 (A = Sc, Ti & V) perovskite-type hydrides: a first principle study," *Chemical Physics*, vol. 568, article 111851, 2023.

[45] H. H. Raza, G. Murtaza, and R. M. Arif Khalil, "Optoelectronic and thermal properties of LiXH3(X =Ba, Sr and Cs) for hydrogen storage materials: a first principle study," *Solid State Communications*, vol. 299, article 113659, 2019.

[46] S. F. A. Shah, G. Murtaza, K. Ismail, H. H. Raza, and I. J. Khan, "First principles investigation of transition metal hydrides LiXH3 (X= Ti, Mn, and Cu) for hydrogen storage," *Journal of Computational Electronics*, vol. 22, no. 4, pp. 921–929, 2023.